ADVANCED OPTICAL MATERIALS
www.advopticalmat.de

Multifunctional Conjugated Ligand with Intimate Binding Improves Luminescence, Charge Transport, and Stability in $CsPbBr_3$ Perovskite Nanocrystals

Jung Min Ha, Nayoung Kim, Dongryeol Lee, Dong Gyu Lee, Ha Yeon Kim, Chang Woo Koh, Ye In Kim, Sungnam Park, Tae Kyung Lee, Myoung Hoon Song,* and Han Young Woo**

Colloidal metal halide perovskite nanocrystals (PNCs) face critical challenges such as poor dispersion stability, ligand desorption, surface defects, and limited charge transport. In this study, a new ligand engineering strategy is introduced using a semiconducting conjugated oligoelectrolyte (COE), QTF2Br, to address these issues in $CsPbBr_3$ PNCs. QTF2Br strongly binds to the PNC surface through bidentate coordination, effectively passivating surface defects and supplying additional bromide ions. This leads to a significantly enhanced photoluminescence quantum yield exceeding 94% and an increase in exciton binding energy from 38.3 to 108.3 meV. Additionally, QTF2Br facilitates Förster resonance energy transfer to the PNC core, functioning as an optical antenna that amplifies green emission by 2.2 times compared to conventional oleic acid/oleylamine-treated PNCs (PNC-OA). The QTF2Br-treated PNCs (PNC-QTF2Br) exhibit improved colloidal stability in polar solvents (e.g., tetrahydrofuran) and retain their PL intensity in toluene for over 7 days. Solid-state films show excellent thermal stability, resisting interparticle aggregation and maintaining clear particle definition. Moreover, the semiconducting nature of QTF2Br enhances charge transport between nanocrystals. This COE-based ligand engineering approach offers a promising solution to overcome key limitations of conventional PNCs for advanced optoelectronic applications.

1. Introduction

Metal halide perovskite nanocrystals (PNCs) have emerged as a promising class of materials for a wide range of optoelectronic applications, owing to their unique and tunable properties. These materials exhibit a number of advantageous characteristics, including ease of solution-based synthesis, strong light absorption, and the ability to fine-tune their electronic band gaps through adjustments in size and composition.[1] In addition, PNCs display high photoluminescence quantum yields (PLQY) and narrow emission spectra, with a full width at half maximum (FWHM) often less than 30 nm. These properties have spurred intense research efforts in areas such as light-emitting devices, lasing, X-ray scintillators, photocatalysis, and photovoltaics.[2] Given their remarkable potential, the field of PNCs continues to be a vibrant area of exploration, with ongoing advancements in both fundamental understanding and practical applications.

A key advantage of PNCs is their compatibility with colloidal solution-based processing, offering a low-cost alternative to high-temperature or vacuum deposition techniques used for solid-state materials. One of the most common synthetic protocols for all-inorganic PNCs ($CsPbX_3$, X = Cl, Br, I) is a hot injection method developed by Protesescu et al., which utilizes oleic acid (OA) and oleyl amine (OAm) as surface-stabilizing ligands.[1a] These long-chain aliphatic ligands are widely adopted not only

J. M. Ha, N. Kim, H. Y. Kim, C. W. Koh, S. Park, H. Y. Woo
Department of Chemistry
Korea University
Seoul 02841, Republic of Korea
E-mail: hywoo@korea.ac.kr

The ORCID identification number(s) for the author(s) of this article can be found under https://doi.org/10.1002/adom.202501640

DOI: 10.1002/adom.202501640

D. Lee, Y. I. Kim, M. H. Song
School of Materials Science and Engineering
Ulsan National Institute of Science and Technology (UNIST)
UNIST-gil 50, Ulsan 44919, Republic of Korea
E-mail: mhsong@unist.ac.kr

D. G. Lee, T. K. Lee
Department of Materials Engineering and Convergence Technology
Gyeongsang National University (GNU)
501 Jinju-daero, Jinju 52828, Republic of Korea
E-mail: tklee8865@gnu.ac.kr

T. K. Lee
School of Materials Science and Engineering
Gyeongsang National University (GNU)
501 Jinju-daero, Jinju 52828, Republic of Korea

to control the growth and shape of the PNCs, but also to ensure colloidal dispersibility, crucially ruling their colloidal characteristics. However, despite their benefits, there are longstanding challenges that limit the practical use of these materials. One significant issue is that the PNCs prepared with a stoichiometric ratio of precursors often exhibit insufficient PLQY (<70%) for actual application, requiring additional treatments (such as introduction of halides) to improve their luminescent properties.[3] Moreover, the aliphatic ligands (e.g., OA, OAm) commonly used for synthesis and surface passivation generally exhibit highly dynamic binding to the PNC surface in the colloidal state.[3a,4] This can lead to ligand desorption over time, resulting in an unstable surface with significant defects or even structural degradation with reduced PLQY. Additionally, PNCs often display inherent instability when exposed to oxygen, moisture, or heat.[5] In such environments, ligands like OA and OAm can detach easily, leading to nanoparticle aggregation and degradation. Furthermore, the long aliphatic chains of these ligands act as electrical insulators, which can significantly hinder charge transport in film and, consequently, degrade the performance of PNCs in practical optoelectronic applications.[6]

To address challenges in PNCs, several strategies have been explored to replace long aliphatic ligands. One approach involves washing PNCs with polar anti-solvents such as methyl acetate (MeOAc) or *N,N*-dimethylformamide (DMF) to remove native ligands and enhance electrical properties.[4a,7] However, this method produces surface defects and reduces PLQY, while ion detachment may decrease stability due to crystal deformation and aggregation. A second strategy uses shorter ligands to promote tunneling effects. For example, Kim et al. synthesized $FAPbBr_3$ PNCs with shorter alkyl chains to improve charge injection.[8] However, shorter ligands can compromise colloidal stability and result in poor-quality films, as well as lead to the formation of low-dimensional perovskites or undesirable geometries.[9] The third approach involves using ligands with aromatic moieties, which can enhance charge injection due to their overlapped π-orbitals.[10] However, their short and rigid structures often reduce nanoparticle solubility, limiting their applicability, especially for larger PNCs. Additionally, aromatic ligands with just one or two benzene rings may not provide sufficient conjugation to significantly improve charge transport. While various strategies have been proposed to improve the performance and stability of PNCs, each approach has its limitations, and further research is needed to identify effective solutions for overcoming these challenges.

Meanwhile, we have explored the use of π-conjugated polyelectrolytes or oligoelectrolytes (CPEs or COEs) as interlayers or charge transport layers in perovskite optoelectronic devices.[11] These conjugated molecules with ionic side chains can enhance charge injection and extraction while providing good wetting and compatibility with the hydrophilic perovskite active layer, with effective interfacial defect passivation. Applying extended π-electron systems to PNC ligands holds significant promise for further delocalizing charges at the PNC surface and enhancing charge transport. CPE or COE structures have great potential to resolve the issues associated with traditional PNC ligands.

Herein, we synthesized a new terfluorene-based cationic COE, QTF2Br, as a multifunctional semiconducting ligand for $CsPbBr_3$ PNCs. We successfully demonstrated that COE ligands effectively modify the surface of $CsPbBr_3$ PNCs, improving their optical and electrical properties, as well as their colloidal, thermal, and solvent stability. The introduction of QTF2Br as a bidentate ligand improved the PLQY through defect passivation and bromide enrichment, while also enabling energy-funneling via Förster resonance energy transfer (FRET). Additionally, temperature-dependent PL analysis revealed a significantly enhanced exciton binding energy in PNCs with QTF2Br ligands (PNC-QTF2Br) compared to conventional OA/OAm-treated PNCs (PNC-OA). The semiconducting ligand structure also improved the charge transport properties of PNC-QTF2Br films, resulting in enhanced hole and electron mobilities. The optical, morphological, dispersion, and electrical properties of PNCs incorporating semiconducting COE ligands were thoroughly studied and compared with those of conventional PNC-OA.

2. Results and Discussion

Figure 1a illustrates the synthetic route to the cationic COE, QTF2Br, which was carefully designed by considering several factors. The terminal quaternary ammonium bromides serve as anchoring groups, enabling strong binding to the PNC surface and passivating defects such as undercoordinated Pb^{2+} ions and A-site vacancies.[12] The large-gap terfluorene backbone is expected to function as an optical antenna, promoting energy transfer and thus enhancing the photoluminescence (PL) of green-emitting $CsPbBr_3$ PNCs.[13] Additionally, the conjugated terfluorene backbone, exhibiting semiconducting properties, improves the electronic characteristics by providing a charge transport pathway. Meanwhile, the ethylhexyl side chains attached to the fluorene core enhance the dispersibility of the PNCs in solutions. 2,7-Dibromo-9,9-bis(4-((6-bromohexyl)oxy)phenyl)-9H-fluorene (M1) and 9,9-bis(2-ethylhexyl)-9H-fluoren-2-pinacolatoboronic ester (M2) underwent a Suzuki–Miyaura cross-coupling reaction using $Pd(PPh_3)_4$ as a catalyst, yielding the charge-neutral terfluorene (TF2) with a 68% yield. To obtain QTF2Br, TF2 was dissolved in tetrahydrofuran (THF) and quaternized with trimethylamine (3.2 M in methanol), resulting in QTF2Br with an 80% yield. The molecular structures of the intermediates and QTF2Br were confirmed by ^1H and ^{13}C NMR, which showed good agreement with the proposed structures (Figures S1–S5, Supporting Information).

UV–vis absorption and PL spectra of the synthesized TF2 and QTF2Br are displayed in Figure 1b. TF2 exhibits an absorption maximum at 353 nm in toluene, while cationic COE, QTF2Br shows the same absorption maximum at 353 nm in 2,2,2-trifluoroethanol (TFE). The PL spectra of both molecules display emissions in the 380–500 nm range, with well-resolved vibronic structures. Their similar UV–vis absorption and PL spectra can be attributed to their identical conjugated backbone. TF2 exhibits a PLQY of 93% in toluene, while QTF2Br achieves ≈90% PLQY in both TFE and dimethyl sulfoxide (DMSO), indicating efficient radiative relaxation for both molecules.[14] According to the cyclic voltammograms of the terfluorenes in Figure 1c, QTF2Br shows oxidation peaks at 0.45 and 0.75 V (vs ferrocene/ferrocenium, Fc/Fc^+), corresponding to the Br^-/Br_3^- and Br_3^-/Br_2 redox couples, respectively, confirming successful incorporation of bromides in QTF2Br.[15] Due to the difficulty of verifying its frontier molecular orbital (FMO) levels via electrochemical analyses,

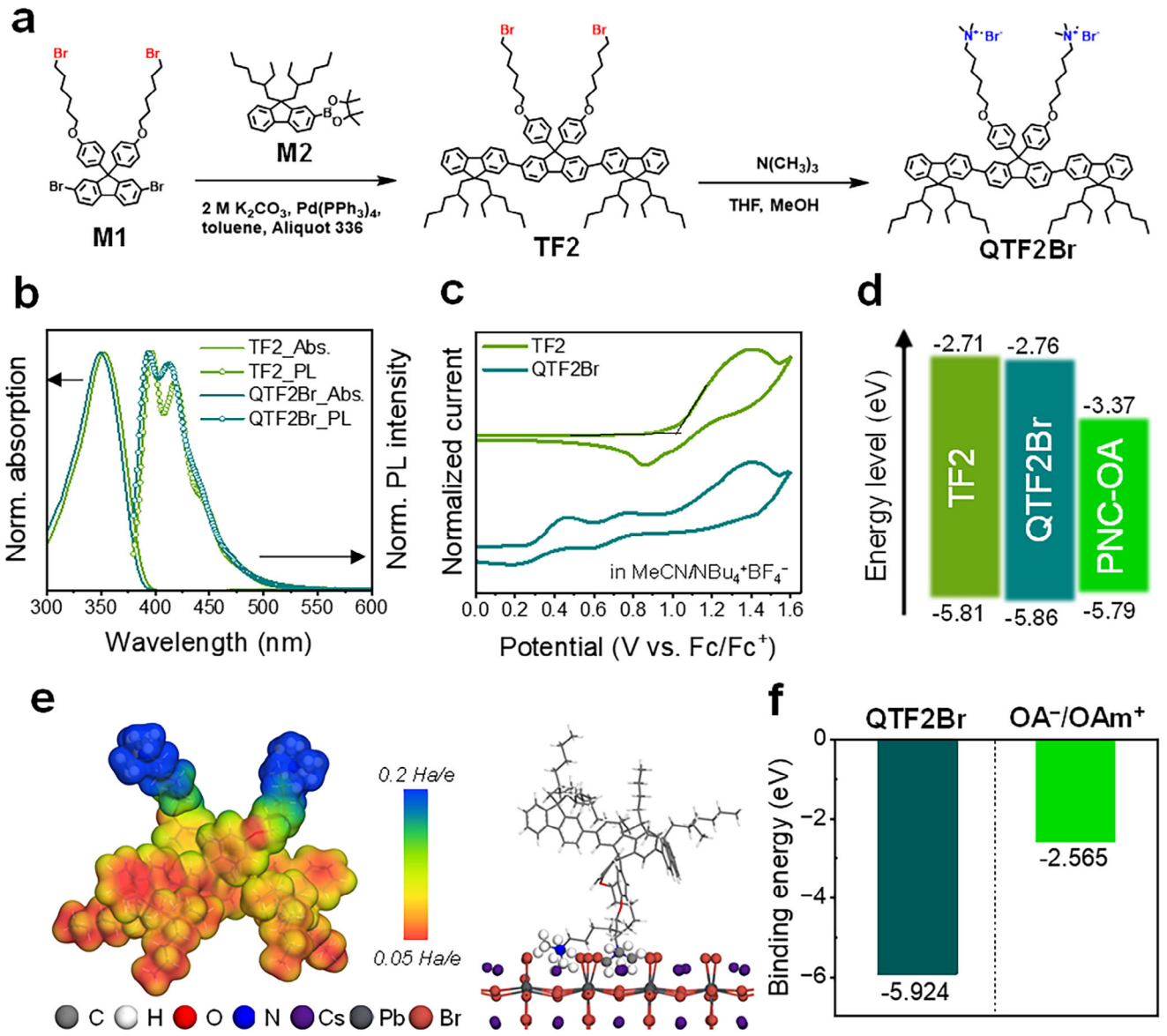

Figure 1. a) Synthetic route to a neutral precursor TF2 and cationic COE, QTF2Br. b) UV–vis absorption and PL spectra of TF2 in toluene and QTF2Br in TFE. c) Cyclic voltammograms of TF2Br and QTF2Br in film. d) Energy level diagram of TF2, QTF2Br, and PNC-OA. e) Electrostatic potential isosurface of QTF2Br (left) and binding geometry on (100) surface of $CsPbBr_3$ perovskite (right). f) Binding energies of QTF2Br and OA^-/OAm^+ ligands on (100) surface of $CsPbBr_3$ perovskite.

the highest occupied molecular orbital (HOMO) and lowest unoccupied molecular orbital (LUMO) levels of QTF2Br films were determined to be −5.86 and −2.76 eV, respectively, using ultraviolet photoelectron spectroscopy (UPS), with the corresponding bandgap estimated from the Tauc plot (Figure 1d; Figure S6, Supporting Information). The results indicate that the FMO levels of QTF2Br closely match those of the neutral precursor TF2, as both share the same conjugated backbone. PNC-OA exhibits valence and conduction band positions at –5.79 and –3.37 eV, respectively. The deeper HOMO level and larger bandgap of QTF2Br relative to the PNCs facilitate efficient energy funneling from QTF2Br to the PNCs. Since the HOMO level of QTF2Br (–5.86 eV) lies deeper than the valence band of $CsPbBr_3$, this energy alignment effectively suppresses undesired back hole transfer from the PNCs to QTF2Br. Together with the strong spectral overlap and close contact between QTF2Br and the PNCs, this configuration enables highly efficient FRET-mediated emission.

To evaluate the ligand capabilities of QTF2Br, density functional theory (DFT) calculations were performed to obtain the electrostatic potential (ESP) isosurface. The results show that the quaternary ammonium moiety carries a strong positive charge, enabling a geometry in which both functional groups can simultaneously interact with the $CsPbBr_3$ surface (Figure 1e). To further investigate this interaction, the binding energy of QTF2Br on the $CsPbBr_3$ (100) surface was compared with that of the conventional OA/OAm ligand system. Based on the ESP

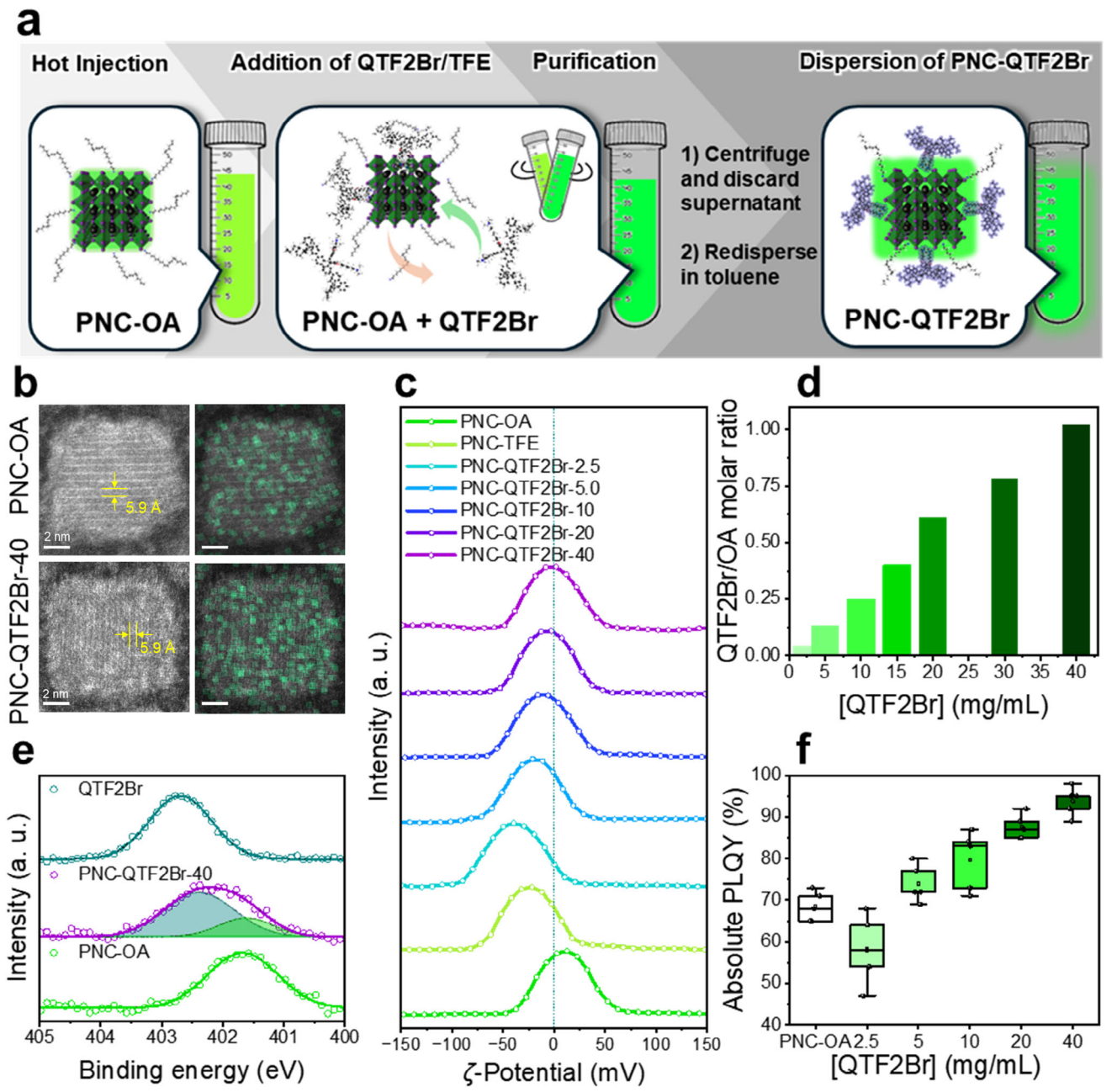

Figure 2. a) Ligand exchange process to produce PNC-COE. b) High-resolution STEM images of PNC-OA and PNCs-QTF2Br-40, c) ζ-potential changes during the ligand exchange process, and d) surface ligand molar ratio of QTF2Br to OA/OAM depending on the treated [QTF2Br] by ^{1}H-NMR measurements. e) N 1s XPS spectra of PNC-OA, PNC-QTF2Br-40, and QTF2Br. f) PLQYs of PNC-QTF2Br in toluene with increasing [QTF2Br] during ligand exchange (obtained from five different samples each).

isosurface of OA^{-}/OAm^{+}, our DFT calculations suggest that the OA^{-}/OAm^{+} pair primarily exists through proton transfer from OAm^{+} to OA^{-}, making it thermodynamically stable (Figure S7, Supporting Information). Furthermore, OA^{-} and OAm^{+} contribute to passivating undercoordinated Pb^{2+} ions and A-site vacancies, respectively, with a binding energy of −2.565 eV. In the case of QTF2Br, the roles of OA^{-} and OAm^{+} are replaced by Br^{-} and -$N(CH_3)_3^{+}$, respectively, forming bidentate coordination with the $CsPbBr_3$ surface. Notably, the binding energy of QTF2Br reaches −5.924 eV, more than twice that of the OA^{-}/OAm^{+} system, highlighting its strong ligand interaction due to dual-site coordination (Figure 1f; Figure S8, Supporting Information).

To synthesize the PNC with QTF2Br as a ligand (PNC-QTF2Br), PNC-OA was first prepared following reported procedures via a hot injection method (see Experimental section).[1a] For the ligand substitution process, TFE was selected as the solvent to dissolve QTF2Br, as outlined in **Figure 2a**. TFE not only serves as a solvent capable of dissolving QTF2Br but also

acts as an orthogonal solvent to perovskites, preventing damage to the crystal phase of $CsPbBr_3$.[16] We observed that PNC-OA treated with pure TFE (PNC-TFE) became more yellowish and turbid compared to the as-prepared PNC-OA. According to transmission electron microscope (TEM) images in Figure S9 (Supporting Information), PNC-OA exhibited cubic crystals with a size of 9 nm, while PNC-TFE showed assembled crystals, with sizes reaching up to 20 nm, due to interparticle merging. The darker surfaces of PNC-TFE suggest that TFE removed the native ligands, thereby enabling the introduction of external ligands. On the other hand, directly adding the QTF2Br solution (in TFE) to the PNC-OA in toluene produced a brighter green-emitting solution, which was distinctly different from PNC-TFE (Figure S10, Supporting Information). Moreover, as the treated concentration of QTF2Br increased, the green emission became more pronounced, indicating that the ammonium bromides function as ligands and bromide sources to stabilize the colloidal PNCs. After mixing PNC-OA (10–12 mg mL^{-1}, 200 µL) with the QTF2Br solution ([QTF2Br] = 2.5–40 mg mL^{-1}, 20 µL), 400 µL of methyl acetate (MeOAc) was added to the mixture to dissolve the detached OA/OAm and precipitate PNC-QTF2Br. The mixture was then centrifuged at 13 500 rpm for 3 min, and the precipitate was re-dispersed in toluene to obtain colloidal PNC-QTF2Br (Figure S11, Supporting Information). TEM images of PNC-QTF2Br-*x*, where *x* is a treated [QTF2Br] in mg/mL, showed that increasing [QTF2Br] helped the PNCs retain their cubic structure with minimal surface etching during ligand exchange (Figure S12, Supporting Information). A comparison of scanning TEM (STEM) images with energy dispersive X-ray (EDX) maps of PNC-OA and PNC-QTF2Br (treated with [QTF2Br] = 40 mg mL^{-1}, PNC-QTF2Br-40) revealed that both PNCs exhibited ~9 nm-sized cubic crystals and a 0.60 Å lattice distance corresponding to the (100) lattice parameter of $CsPbBr_3$. However, PNC-QTF2Br shows a higher content of Br^- on the surface due to the external Br^- supply from QTF2Br (Figure 2b; Figure S13, Supporting Information). X-ray diffraction (XRD) spectra also indicate that the crystal phase of $CsPbBr_3$ is retained after the ligand exchange process (Figure S14, Supporting Information).

To assess the surface charge and corresponding dispersibility of the colloidal PNCs after ligand exchange, ζ-potential measurements were conducted (Figure 2c). The ζ-potential of PNC-OA was +12.3 mV, while PNC-TFE exhibited a negative charge of −22.3 mV due to the exposure of negatively charged Br− following the removal of native ligands. Upon treatment of PNC-OA with 2.5 mg mL^{-1} of QTF2Br, the ζ-potential became negative, likely due to insufficient ligand and surface passivation, resulting in halide exposure. As the concentration of QTF2Br increased, the ζ-potential gradually approached zero, eventually reaching +1.54 mV for PNC-QTF2Br-40, indicating a stably dispersed state in a non-polar medium. To assess the ligand ratio of QTF2Br to OA/OAm after ligand exchange, ^1H nuclear magnetic resonance (NMR) was performed on purified (and dried) PNCs dissolved in DMSO-d_6 (Figure 2d; Figure S15 and Table S1, Supporting Information). The NMR spectra display the phenyl proton signals of QTF2Br (H_a) between 6.5–7.0 ppm and vinyl proton signals of OA/OAm (H_b) at 5.3 ppm, allowing for a comparison of the respective peak integrals. The molar ratio of QTF2Br to OA/OAm increased linearly with rising [QTF2Br] during the ligand exchange process, reaching a molar ratio of 1.02:1 for PNC-QTF2Br-40.

To further investigate the ligand exchange in PNC-QTF2Br, X-ray photoelectron spectroscopy (XPS) was conducted. The N 1s XPS spectrum of PNC-QTF2Br-40 in Figure 2e and Figure S16 (Supporting Information) reveals two distinct peaks: one at 401.7 eV, corresponding to oleyl ammonium (—NH_3^+), and another at 402.6 eV, attributed to the quaternary ammonium (—$N(CH_3)_3^+$) groups in QTF2Br, confirming the coexistence of both ligands.[17] Figure S16a (Supporting Information) presents the Pb 4f XPS spectra, where PNC-OA displays a Pb $4f_{7/2}$ peak at 138.3 eV, which shifts to a lower binding energy of 138.0 eV upon introducing 40 mg mL^{-1} of QTF2Br. This suggests that bromide ions (Br^-) in QTF2Br strongly bind to the surface undercoordinated Pb^{2+} via a Lewis acid-base interaction. The Br 3d XPS spectra show that the characteristic $3d_{5/2}$ peak of Br^- from unbound QTF2Br (at 67.6 eV) shifts to 68.2 eV in all PNC-QTF2Br samples, indicating that the bromide ions from QTF2Br participated in constructing the PNC surface.

The UV–vis absorption spectrum of PNC-QTF2Br in toluene shows a notable increase in absorption ≈360 nm, which corresponds to the absorption of COEs (Figure S17, Supporting Information). Meanwhile, the green PL spectra of the $CsPbBr_3$ PNCs exhibited no significant peak shift or FWHM broadening after treatment with QTF2Br, as shown in Figure S17b (Supporting Information). The absolute PLQY of colloidal PNC-QTF2Br in toluene was evaluated with varying [QTF2Br] (Figure 2f; Table S1, Supporting Information). The sample treated with [QTF2Br] = 2.5 mg mL^{-1} (PNC-QTF2Br-2.5) exhibited a reduced PLQY, but the PLQY progressively increased with higher concentrations of [QTF2Br], reaching a maximum of ≈94% for PNC-QTF2Br-40. This concentration was set as the optimal condition for further analysis. As discussed above, the QTF2Br COE ligands (HOMO: −5.86 eV, LUMO: −2.76 eV, bandgap: 3.1 eV) feature a terfluorene-based structure and exhibit semiconducting properties with deep blue PL emission in the 380-500 nm range, which overlaps with the broad absorption of $CsPbBr_3$. The energy levels of $CsPbBr_3$ PNCs (HOMO: −5.79 eV, LUMO: −3.37 eV, bandgap: 2.42 eV) lie between those of QTF2Br. This energy level alignment, along with the spectral overlap, strongly suggests the possibility of FRET from QTF2Br to $CsPbBr_3$, leading to FRET-mediated PL enhancement in PNC-QTF2Br. FRET is a nonradiative energy transfer mechanism mediated by dipole-dipole coupling, which depends on both the spectral overlap between the donor emission and acceptor absorption, as well as the intermolecular distance ($\propto 1/d^6$).[12a,18] Unlike physically blended FRET donors, QTF2Br can act as a surface ligand that is chemically bound to the PNC surface via bidentate coordination. This intimate spatial proximity between the donor (QTF2Br) and acceptor ($CsPbBr_3$ PNC) allows for a significantly reduced donor–acceptor distance (within ≈1 nm), which is a key parameter in the FRET efficiency. Therefore, QTF2Br enables not only efficient energy transfer in solution but also in colloidal and solid-state systems due to its dual functionality as both a ligand and a donor fluorophore. As displayed in **Figure 3a**, under 360 nm excitation, PNC-QTF2Br exhibits a fluorescence intensity at 513 nm that is 2.2 times higher than that of PNC-OA, confirming that photoexcited QTF2Br contributes to exciton generation in the PNCs via efficient FRET. To investigate this phenomenon, we

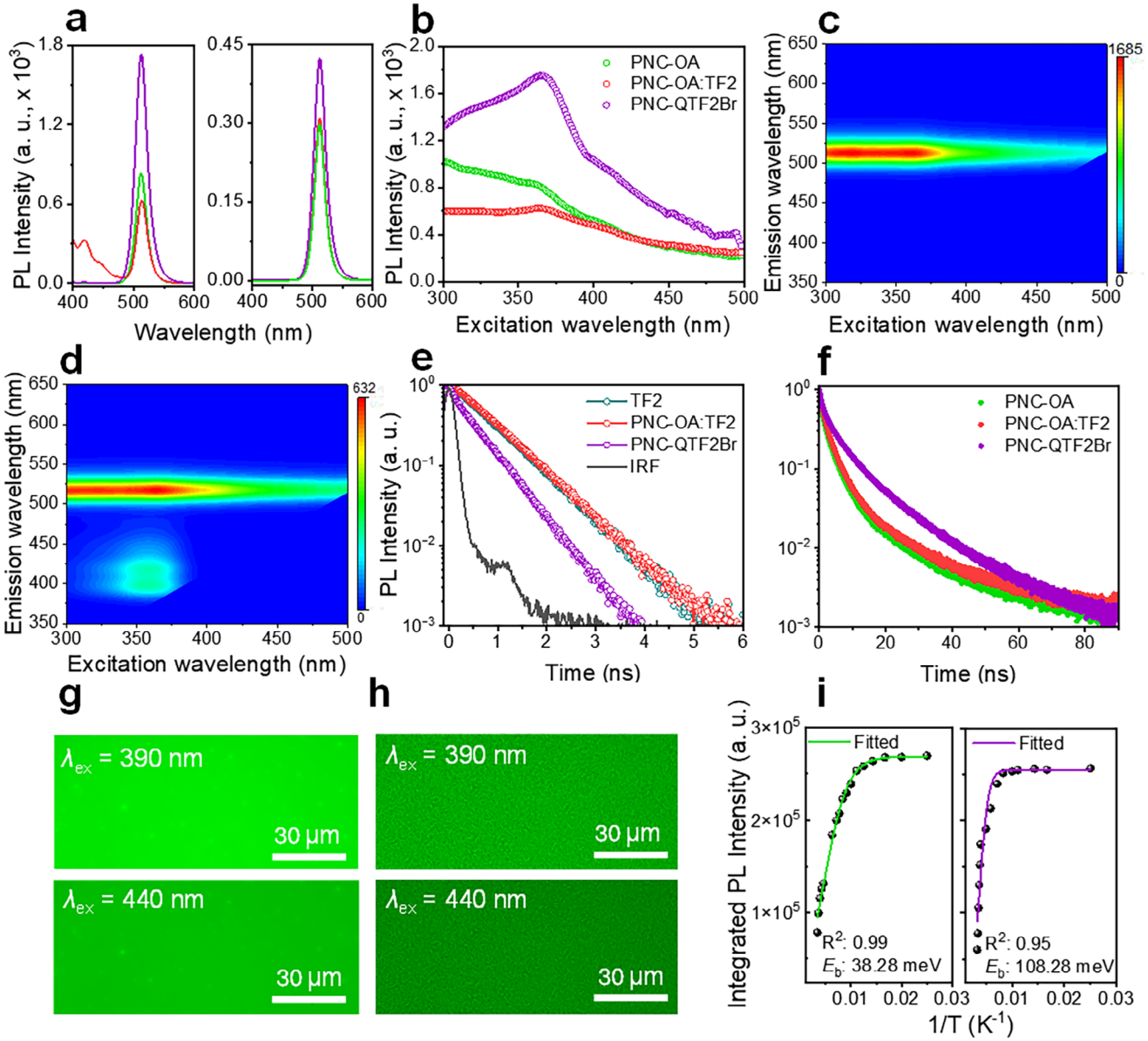

Figure 3. a) PL spectra of PNCs by exciting at 360 nm (left) and 450 nm (right). PNC-OA (green), PNC-OA:TF2 (orange), and PNC-QTF2Br-40 (magenta). b) PLE spectra of colloidal PNC-OA, PNC-OA:TF2, and PNC-QTF2Br-40 solution in toluene. Detected at 513 nm. 2D PLE contour spectra of c) PNC-QTF2Br-40 and d) PNC-OA:TF2 in toluene. TRPL decay profiles of TF2, PNCs-OTF2Br-40, and PNC-OA: TF2 colloidal solution measured at a detection wavelength of 418 nm e) and 513 nm f) (excitation at 375 nm). Fluorescent microscopic images of g) PNC-QTF2Br-40 and h) PNC-OA films by exciting at 390 nm (FRET-mediated PL) and 440 nm (PL by direct excitation of $CsPbBr_3$). i) Temperature-dependent PL intensity measurements and calculated exciton binding energy of PNC-OA (left) and PNC-QTF2Br-40 (right).

also analyzed the photoluminescence excitation (PLE) spectrum of the colloidal PNC-QTF2Br-40 solution by measuring the PL intensity at 513 nm by varying the excitation wavelength (λ_{ex}) from 300 to 500 nm (Figure 3b–d; Figures S18–S20, Supporting Information). The PLE spectrum of PNC-OA closely matches its UV–vis absorption spectrum, while that of PNC-QTF2Br exhibits significantly enhanced PL emission in a range of λ_{ex} = 300–500 nm, with the highest PL intensity observed at λ_{ex} = 360 nm, which corresponds to the λ_{abs} of QTF2Br (Figure 3b). The 2D PLE spectrum of PNC-QTF2Br shows no PL signal from QTF2Br itself at any λ_{ex}, indicating efficient FRET from QTF2Br to the PNCs (Figure 3c). This clearly contrasts with the 2D PLE spectrum of a PNC-OA:TF2 (neutral precursor of QTF2Br) mixture, in which a distinct fluorescence signal from TF2 (suggesting no interaction between PNC-OA and TF2) is observed upon excitation at λ_{ex} = 320–380 nm, where TF2 exhibits strong absorption (Figure 3d; Figure S18, Supporting Information). Additionally, PL spectra of both PNC-OA and PNC-QTF2Br were recorded under direct excitation of the PNCs at λ_{ex} = 450 nm, where neither QTF2Br nor OA absorbs, and their optical densities are nearly identical. Interestingly, the PL intensity of PNC-QTF2Br was 1.4 times higher than that of PNC-OA. This

enhancement is attributed to surface defect passivation and halide enrichment by the COEs, which aligns well with the improved PLQY of PNCs treated with QTF2Br (from 68% to 94%). Consequently, the enhanced green PL observed in PNC-QTF2Br arises from the synergistic effects of FRET and defect passivation facilitated by QTF2Br ligands on the PNC surfaces.

Furthermore, transient photoluminescence (TRPL) spectra were measured to analyze the PL lifetimes (τ) of QTF2Br ligands and PNC-QTF2Br. The PL decay profiles were collected at 418 nm (corresponding to QTF2Br emission) and 513 nm (PNC emission) under 375 nm excitation, which closely matches the λ_{abs} of QTF2Br. Since QTF2Br is insoluble in toluene, TF2 was used as a control to assess the extent of τ reduction for QTF2Br in the presence of $CsPbBr_3$ PNCs. To confirm that the τ values of TF2 and QTF2Br are comparable, we measured their PL decay profiles in the same medium (toluene:TFE = 10:1, by volume), where both were soluble and exhibited similar PL spectra, with τ values at 418 nm of 0.97 ns for TF2 and 0.98 ns for QTF2Br; virtually identical (Figure S21, Supporting Information). As shown in Figure 3e, the average τ of QTF2Br in PNC-QTF2Br at 418 nm was significantly shorter (0.50 ns) than that of TF2 (0.84 ns), indicating efficient quenching of QTF2Br emission by the PNCs. This reduction in τ for PNC-QTF2Br is attributed to efficient FRET from the QTF2Br ligands to the PNC core. In contrast, PNC-OA:TF2 exhibited a negligible change in τ (≈0.87 ns), indicating no FRET due to the large separation between TF2 and the PNCs. Based on the measured τ values, the FRET rate ($k_{FRET} = \frac{1}{\tau_{PNC-QTF2Br}} - \frac{1}{\tau_{TF2}}$) and efficiency ($\eta_{FRET} = (1 - \frac{\tau_{PNC-QTF2Br}}{\tau_{TF2}}) \times 100$), where k_{FRET} represents the FRET rate, η_{FRET} is the FRET efficiency, and the τ values correspond to the PL lifetimes of the donor (TF2) and the donor-acceptor resonance system (PNC-QTF2Br), respectively.[19] According to the calculation, k_{FRET} of η_{FRET} of PNC-QTF2Br were estimated to be ≈0.85 ns^{-1} and 43%, respectively. Additionally, the PL decays of PNC-OA and PNC-QTF2Br at λ_{PL} = 513 nm were monitored under excitation of the PNCs at 375 nm (Figure 3f; Table S2, Supporting Information). PNC-OA in toluene exhibited an average τ of 7.66 ns, while PNC-QTF2Br displayed an extended lifetime of 9.95 ns, primarily attributed to bromide supply and surface passivation by the QTF2Br ligands, which aligns well with the steady-state PL measurements. Fluorescence microscopy images in Figure 3g,h further support the FRET-mediated brighter green emission at λ_{ex} = 390 nm in PNC-QTF2Br films compared to PNC-OA films. Similarly, brighter fluorescence images of PNC-QTF2Br films under direct excitation of $CsPbBr_3$ PNC (λ_{ex} = 440 nm) were also obtained. The TRPL decay profiles of the PNC films confirm that PNC-QTF2Br exhibits a significantly improved average PL lifetime (τ_{avr} = 8.82 ns) compared to PNC-OA (τ_{avr} = 2.45 ns), indicating enhanced excitonic radiative decays originating from reduced defects and non-radiative recombination in PNC-QTF2Br films (Figure S22 and Table S3, Supporting Information).

Grazing incidence wide-angle X-ray scattering (GIWAXS) was performed to compare the morphology of PNC films with varying concentrations of QTF2Br ligands (Figures S23 and S24, Supporting Information). PNC-OA films exhibit a pronounced scattering peak at q = 1.06 $Å^{-1}$ (d = 5.95 Å) in both the out-of-plane and in-plane directions, corresponding to the (100) lattice plane of $CsPbBr_3$. This indicates a well-ordered cubic orientation. PNC-QTF2Br films show improved nanocrystal alignment with increasing [QTF2Br], which is attributed to enhanced surface integrity due to QTF2Br treatment. In Figure S25 (Supporting Information), scanning electron microscopy (SEM) images reveal that PNC-OA films form supercrystals of 100–200 nm in size with voids between them, whereas PNC-QTF2Br-40 films exhibit smaller, well-defined crystallites and smoother surfaces. While supercrystal formation is known to enhance charge transport, a high density of surface defects within the superlattice can induce structural rearrangement and deformation at the interfaces due to ripening, leading to a lower exciton binding energy or PL quenching.[20] This suggests that COE-induced interparticle separation at interfaces can more favorably enhance radiative recombination by suppressing agglomeration. Temperature-dependent PL analysis also confirms a significantly higher exciton binding energy (E_b) for PNC-QTF2Br (108.28 meV) compared to PNC-OA (38.28 meV), further supporting its superior emissive properties (Figure 3i). The confocal microscopic images in Figure S26 (Supporting Information) further confirm the enhanced radiative recombination along the PNC-QTF2Br film surface.

The colloidal stability of PNCs is crucial for their practical applications, as they are highly sensitive to environmental factors such as moisture, solvent polarity, and temperature.[21] These factors can lead to rapid degradation of their structural integrity or, conversely, induce crystal ripening and aggregation through ion diffusion and rearrangement.[22] To protect them from external stimuli, ligands must play a key role. The stability of PNCs is strongly dependent on the binding affinity of ligands, as the system remains dynamic, leading to the detachment of weakly bound ligands. To evaluate the colloidal stability of PNC-QTF2Br in toluene, we first tracked the PL spectra of the respective colloidal solution for ≈7 days under ambient conditions (**Figure 4a**; Figures S27 and S28, Supporting Information). To introduce a quaternary ammonium-type monofunctional ligand with a single aromatic ring as a control, we prepared PNCs treated with benzyldodecyldimethylammonium bromide (PNC-BDAB) using the same synthetic protocol as PNC-QTF2Br (see Experimental Section). As shown in Figure 4a, PNC-OA dispersed in toluene exhibited a sharp decrease to 20% of its initial PL intensity after just one day of storage under ambient conditions. This was accompanied by a shift in the maximum PL wavelength (λ_{PL}) from 513 to 516 nm, indicating poor surface stability and interparticle aggregation. In contrast, PNC-QTF2Br in toluene showed significantly improved stability, maintaining its initial PL intensity over 7 period. PNC-BDAB retained over 90% of its initial PL intensity after two days but exhibited significantly lower stability than PNC-QTF2Br. These results suggest that PNCs adopting the monofunctional ligand may undergo aggregation or degradation even in a nonpolar solvent like toluene, but the stability can be noticeably enhanced by the bidentate, extended aromatic QTF2Br ligand. We also tested the stability in a more polar solvent, tetrahydrofuran (THF), under N_2 conditions to assess the effect of solvent polarity on colloidal stability (Figure 4b; Figures S29 and S30, Supporting Information). PNC-OA rapidly degraded in THF within an hour, losing its luminescent property and forming a yellow phase. Although PNC-BDAB exhibited better stability in THF compared to PNC-OA, it also lost its PL property completely within 36 h. In contrast, PNC-QTF2Br exhibited

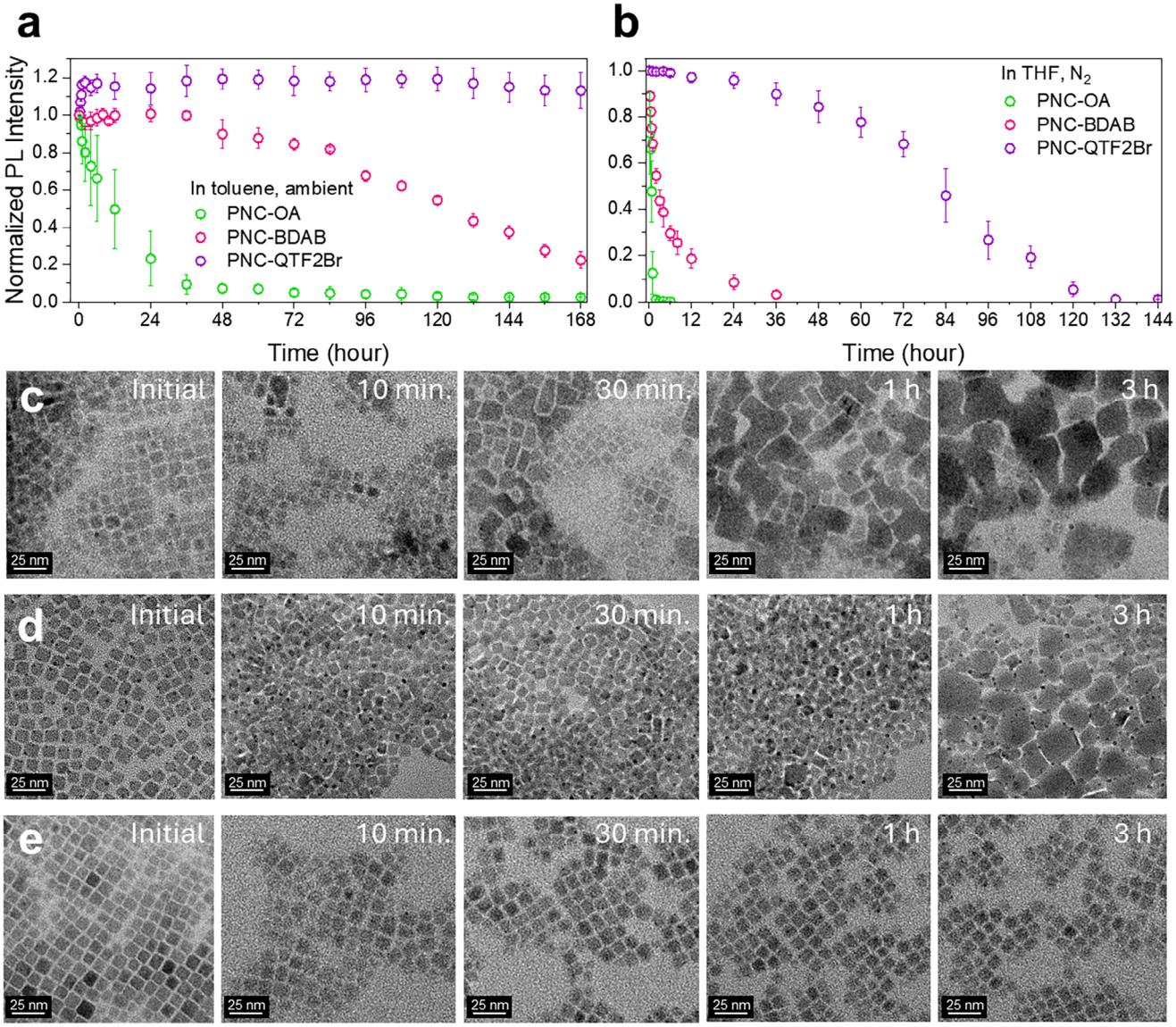

Figure 4. PL intensity tracking of colloidal PNC-OA, PNC-BDAB, PNC-QTF2Br-40 in toluene a) and THF b) (independently obtained from five samples each). TEM images of c) PNC-OA, d) PNC-BDAB, and e) PNC-QTF2Br-40 by increasing heating time at 100 °C in air.

superior stability compared to the other two PNCs, even in THF, maintaining 80% of its initial intensity after 48 h. Specifically, as shown in Figure S30d (Supporting Information), both PNC-OA and PNC-BDAB underwent degradation in THF, exhibiting a redshift in λ_{PL} beyond 520 nm, whereas PNC-QTF2Br showed only a minimal shift. The DFT calculations of the binding energies of each ligand molecule on $CsPbBr_3$ in toluene ($\varepsilon = 2.37$) and THF ($\varepsilon = 7.43$) environments revealed that, despite the high dielectric constant of THF, QTF2Br exhibited the highest binding affinity (Figure S31, Supporting Information). The stability of PNC-QTF2Br in THF suggests that the conjugated structure of the COE contributes to enhanced colloidal stability, even in polar media, by providing more effective surface protection than aliphatic or monoaromatic ammonium bromide ligands.

Thermal stress can also degrade PNCs by accelerating ion diffusion within their crystal structure; however, surface protection can help mitigate thermal degradation and maintain their structural integrity. To assess this effect, we heated spin-coated PNC films (≈50 nm thick) at 100 °C and monitored the PL emission at 1-h intervals in ambient air (Figure S32, Supporting Information). PNC-OA and PNC-BDAB exhibited complete PL loss after 6 h of cumulative heating, while PNC-QTF2Br demonstrated significantly improved thermal stability. To further investigate the degradation process of PNCs under heat, we monitored the nanoparticles using TEM at various heating times. As shown in Figure 4c, prolonged heating (~30 min) caused the particles of PNC-OA to collapse at the edges, eventually forming irregular, round-shaped particles with numerous defect sites and fused particles. For PNC-BDAB, thermal stability was slightly improved compared to PNC-OA; however, crystal degradation became noticeable after 3 h (Figure 4d). In contrast, Figure 4e shows that PNC-QTF2Br significantly enhanced surface definition,

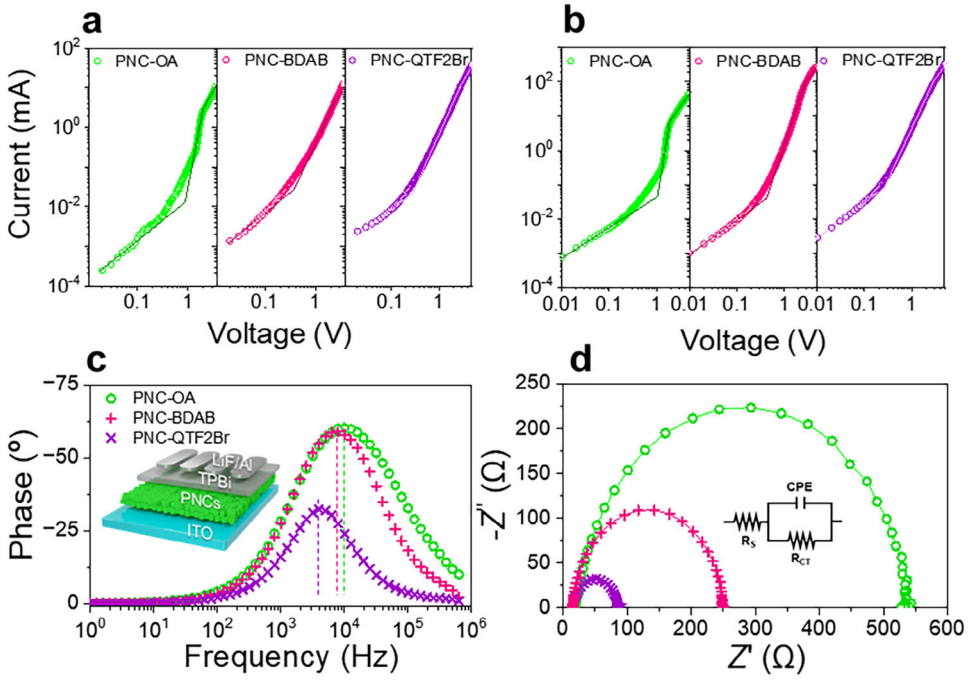

Figure 5. *J-V* characteristics of a) electron-only and b) hole-only devices of PNC-OA, PNC-BDAB, and PNC-QTF2Br-40. c) Bode plots and d) Nyquist plots of EIS measurements of PNC-OA, PNC-BDAB, and PNC-QTF2Br-40 films with a device architecture of ITO/PNCs/TPBi/LiF/Al. The insets show the corresponding cell architecture and the Randles circuit model.

retaining its shape and size even after 3 h of heating. It was only after 5 h of heating that ripening occurred in PNC-QTF2Br, leading to the partial formation of larger particles (Figure S33, Supporting Information). These results suggest that PNC-QTF2Br demonstrates excellent particle definition and surface stabilization, effectively preventing ion diffusion between particles even in the solid state.

The final motivation for incorporating the COE ligand with extended conjugation is to replace the insulating interface with a semiconducting exterior, thereby enhancing charge transport across the PNCs. To validate the charge transport enhancement effect of the COE ligands, dark current measurements were conducted on electron-only devices (ITO/SnO_2/PNCs/2,2′,2′′-(1,3,5-benzinetriyl)-tris(1-phenyl-1-H-benzimidazole) (TPBi)/LiF/Al) and hole-only devices (ITO/PEDOT:PSS/PNCs/MoO_3/Au) (**Figure** 5a,b Figure S34 and Table S4, Supporting Information). In the trap-free space charge limited current (SCLC) regime, the electron and hole mobilities for both types of devices were determined using the Mott-Gurney Equation (1),[23]

$$J = \frac{9\varepsilon_0\varepsilon_r\mu V_b^2}{8L^3} \quad (1)$$

where J is the current density, ε_0 is the vacuum permittivity, ε_r is the relative dielectric constant (ε_r for $CsPbBr_3$ = 22), μ is the mobility, V_b is the applied voltage, and L is the thickness of PNC films.[24] For PNC-OA, the electron mobility (μ_e) and hole mobility (μ_h) were 9.89×10^{-5} and 1.93×10^{-4} cm^2 V^{-1} s^{-1}, respectively, while PNC-BDAB showed enhanced mobilities due to the contribution of π orbitals along the aromatic ring ($\mu_e = 1.25 \times 10^{-4}$ and $\mu_h = 9.97 \times 10^{-4}$ cm^2 V^{-1} s^{-1}). In the case of both PNC-QTF2Br, μ_e (1.77×10^{-4} cm^2 V^{-1} s^{-1}) and μ_h (1.42×10^{-3} cm^2 V^{-1} s^{-1}) exhibited the highest values among the three PNCs, demonstrating a greater enhancement in charge transport compared to the BDAB-treated PNCs. Additionally, the trap-filled limit voltages (V_{TFL}) of the electron-only devices (0.86, 0.46, and 0.27 V for PNC-OA, PNC-BDAB, and PNC-QTF2Br, respectively) and hole-only devices (1.06, 0.42, and 0.25 V, respectively) indicate a significantly reduced trap density with QTF2Br treatment.

Electrical impedance spectroscopy (EIS) was also performed on PNC-OA, PNC-BDAB, and PNC-QTF2Br films (Figure 5c,d; Figure S35, Supporting Information) with a sandwich cell structure of ITO/PNC/TPBi/LiF/Al. According to the Bode plot in Figure 5c and Figure S34 (Supporting Information), the maximum phase transition frequency progressively decreased from 10,000 Hz for PNC-OA to 7943 Hz for PNC-BDAB and 3981 Hz for PNC-QTF2Br. The maximum phase shift angle was significantly reduced for PNC-QTF2Br (−32.30°) compared to PNC-OA (−60.00°), suggesting that the introduction of QTF2Br effectively suppressed capacitive charge accumulation at the interface, leading to more efficient charge transport across the PNC layer. The corresponding Nyquist plot also suggests that the charge transfer resistance (R_{CT}) for PNC-OA was 535 Ω, which decreased to 248 Ω with BDAB treatment, indicating improved interfacial charge transfer upon replacing OA with BDAB. For PNC-QTF2Br, a significant reduction in R_{CT} was observed (86 Ω), suggesting further suppressed interfacial resistance due to the incorporation of the COE with extended π-conjugation. The EIS and SCLC measurements consistently indicate that the COE ligand with extended conjugation enhances interfacial charge transfer and transport characteristics. To assess the influence of surface ligands on interparticle charge transport, we

measured the electrical conductivity of PNC films using the four-point probe method (Figure S36, Supporting Information). The conductivity increased from 1.09×10^{-8} S cm^{-1} for PNC-OA to 6.38×10^{-7} S cm^{-1} for PNC-BDAB, and further higher to 4.93×10^{-6} S cm^{-1} for PNC-QTF2Br. This trend confirms that ligand exchange enhances charge transport by improving interparticle coupling. Notably, QTF2Br results in higher conductivity than BDAB, suggesting that its extended conjugated core contributes to the improved electrical properties of the PNC film. These results show that the COE ligand not only reduces trap-mediated charge localization but also improves interparticle electronic communication, contributing to more stable and efficient charge transport.

3. Conclusion

In this work, we successfully demonstrated that COE ligands can act as effective multifunctional surface modifiers for $CsPbBr_3$ PNCs, leading to significantly improved optical and electrical properties, while also enhancing colloidal, thermal, and solvent stability. The introduction of QTF2Br as a bidentate ligand not only enhanced the PLQY through defect passivation and bromide enrichment but also enabled an energy-funneling effect via FRET. Notably, PNC-QTF2Br exhibited a 2.2-fold increase in PL intensity upon 360 nm excitation compared to conventional PNC-OA, demonstrating efficient FRET-mediated energy transfer and PL amplification. Furthermore, the significantly improved dispersion stability in polar solvents and morphological stability in films are also noteworthy. The semiconducting conjugated ligand structure and reduced trap density further contributed to enhanced charge transport, with an electron mobility (μ_e) of 1.77×10^{-6} cm^2/ V^{-1} s^{-1} and hole mobility (μ_h) of 1.42×10^{-3} cm^2 V^{-1} s^{-1}, as confirmed by EIS and SCLC measurements. Additionally, temperature-dependent PL analysis revealed an exciton binding energy of 108.28 meV, significantly higher than that of PNC-OA (38.28 meV), indicating enhanced exciton confinement and reduced nonradiative recombination. The results show that the extended conjugated structure of QTF2Br contributes more significantly to enhancing the photoelectrical properties of PNCs than a single aromatic ring, as seen in PNC-BDAB. These findings provide a new perspective on ligand engineering for PNCs, demonstrating the great potential of COE-based surface modification for practical applications in PNC-based optoelectronic devices. Overall, the QTF2Br ligand enables robust defect passivation while simultaneously providing a semiconducting interface that facilitates efficient charge transport in PNC films. These combined optical and electrical advantages underscore the strong potential of QTF2Br for high-performance optoelectronic devices such as LEDs.

4. Experimental Section

Materials: Cs_2CO_3 (>99%), $PbBr_2$ (>99%), ODE (>91%), OAm (70%, technical grade), OA (90%, technical grade), BDAB (≥99%), all solvents, and all the reagents for the synthesis of COE were purchased from Sigma Aldrich and Tokyo Chemical Industry. PEDOT:PSS (AI 4083) and TPBi were purchased from OSM. MoO_3 and Al were purchased from iTASCO. SnO_2 was purchased from Alfa Aesar.

PNC-OA: The colloidal solution of $CsPbBr_3$ PNC-OA was synthesized following the reported hot injection method.[1a] $PbBr_2$ (0.552 g) and 40 mL of ODE were loaded into a 3-neck round-bottom flask and degassed under vacuum at 120 °C for 1 h. Under an N_2 atmosphere, 4 mL of OA and 4 mL of OAm were added to the degassed $PbBr_2$ mixture, followed by further degassing at 180 °C for 30 min. Separately, a mixture of Cs_2CO_3 (0.407 g), 1.25 mL of OA, and 20 mL of ODE was placed in a flask and degassed under vacuum at 130 °C for 2 h. After degassing, the temperature was increased to 150 °C under vacuum to ensure complete conversion of Cs_2CO_3 to Cs-oleate. To synthesize PNC-OA, 3.2 mL of the hot Cs-oleate solution was quickly injected into the prepared $PbBr_2$ solution at 180 °C. After 5 s of stirring, the reaction flask was rapidly cooled in an ice bath, yielding crude green PNC-OA in ODE.

Purification of PNC-OA: The crude PNC-OA in ODE was transferred to a centrifugal tube and centrifuged at 10 000 rpm for 10 min. After centrifugation, the supernatant was discarded to remove excess ligands, salts, and undersized $CsPbBr_3$ nanocrystals. The precipitate was then dispersed in 6 mL of hexane, followed by the immediate addition of 12 mL of MeOAc. The mixture was shaken several times to form a turbid solution. After centrifuging the mixture at 10 000 rpm for 3 min, the supernatant was removed, and the precipitate was redispersed in 8 mL of toluene. The PNC-OA dispersed in toluene was then obtained from the supernatant by centrifuging the solution at 4 000 rpm. The concentration of the resulting stock solution was measured to be 10–12 mg mL^{-1}, with an absorbance of 1.0–1.2 at 300 nm after diluting it 1:300 with toluene.

PNC-QTF2Br and PNC-BDAB: In an N_2-filled glove box, the as-prepared PNC-OA (10–12 mg mL^{-1}, 200 µL) in toluene was mixed with 20 µL of QTF2Br in TFE (with concentrations ranging from 2.5 to 40 mg mL^{-1}) and vortexed for 3 min. The color of the PNC solution immediately changed to a brighter green after the addition of the QTF2Br solution (with [QTF2Br] greater than 5 mg mL^{-1}). Next, 400 µL of MeOAc was added to the mixture and gently shaken until it formed a turbid suspension, followed by centrifugation at 13 500 rpm for 3 min. The precipitate was then redispersed in 200 µL of toluene to produce a stock solution of PNC-QTF2Br. For PNC-BDAB, a BDAB solution in TFE was prepared similarly. A 19.6 mg mL^{-1} solution of BDAB in TFE was used for ligand exchange, which contains an equivalent molar amount of Br− (51.0 mM) to the 40 mg mL^{-1} QTF2Br solution.

Supporting Information

Supporting Information is available from the Wiley Online Library or from the author.

Acknowledgements

J.M.H., N.K., D.L., and D.G.L. contributed equally to this work. This work was supported by the National Research Foundation (NRF) grants funded by the Ministry of Science and ICT (MSIT), the Korean government (RS-2024-00334832 and RS-2025-00514448). This work was supported by Samsung Research Funding & Incubation Center of Samsung Electronics under Project Number SRFC-TC2103-01. This work was also supported by the Technology Innovation Program Development Program funded by the Ministry of Trade, Industry & Energy (MOTIE) (RS-2023-00265858).

Conflict of Interest

The authors declare no conflict of interest.

Data Availability Statement

The data that support the findings of this study are available in the supplementary material of this article.

Keywords

colloidal stability, conjugated ligands, conjugated oligoelectrolytes, energy transfer, metal halide perovskites

Received: May 22, 2025
Revised: August 22, 2025
Published online:

[1] a) L. Protesescu, S. Yakunin, M. I. Bodnarchuk, F. Krieg, R. Caputo, C. H. Hendon, R. X. Yang, A. Walsh, M. V. Kovalenko, *Nano Lett.* **2015**, *15*, 3692; b) M. V. Kovalenko, L. Protesescu, M. I. Bodnarchuk, *Science* **2017**, *358*, 745; c) J. Shamsi, A. S. Urban, M. Imran, L. De Trizio, L. Manna, *Chem. Rev.* **2019**, *119*, 3296; d) Q. A. Akkerman, V. D'Innocenzo, S. Accornero, A. Scarpellini, A. Petrozza, M. Prato, L. Manna, *J. Am. Chem. Soc.* **2015**, *137*, 10276; e) A. Dey, J. Ye, A. De, E. Debroye, S. K. Ha, E. Bladt, A. S. Kshirsagar, Z. Wang, J. Yin, Y. Wang, L. N. Quan, F. Yan, M. Gao, X. Li, J. Shamsi, T. Debnath, M. Cao, M. A. Scheel, S. Kumar, J. A. Steele, M. Gerhard, L. Chouhan, K. Xu, X. Wu, Y. Li, Y. Zhang, A. Dutta, C. Han, I. Vincon, A. L. Rogach, et al., *ACS Nano* **2021**, *15*, 10775.

[2] a) Y.-H. Kim, T.-W. Lee, *Acc. Mater. Res.* **2023**, *4*, 655; b) Q. Zhang, Q. Shang, R. Su, T. T. H. Do, Q. Xiong, *Nano Lett.* **2021**, *21*, 1903; c) Z. Yang, J. Yao, L. Xu, W. Fan, J. Shang, *Nat. Commun.* **2024**, *15*, 8870; d) J. Wang, Y. Shi, Y. Wang, Z. Li, *ACS Energy Lett.* **2022**, *7*, 2043; e) G. R. Yettapu, D. Talukdar, S. Sarkar, A. Swarnkar, A. Nag, P. Ghosh, P. Mandal, *Nano Lett.* **2016**, *16*, 4838; f) H. Choi, H. Kim, J. Lim, B.-J. Chang, S. Song, *Macromol. Res.* **2024**, *32*, 825; g) J. Luo, J. Li, L. Grater, R. Guo, A. R. bin Mohd Yusoff, E. Sargent, J. Tang, *Nat. Rev. Mater.* **2024**, *9*, 282.

[3] a) L. De Trizio, I. Infante, L. Manna, *Acc. Chem. Res.* **2023**, *56*, 1815; b) Y. Dong, T. Qiao, D. Kim, D. Parobek, D. Rossi, D. H. Son, *Nano Lett.* **2018**, *18*, 3716; c) M. Imran, V. Caligiuri, M. Wang, L. Goldoni, M. Prato, R. Krahne, L. De Trizio, L. Manna, *J. Am. Chem. Soc.* **2018**, *140*, 2656.

[4] a) J. De Roo, M. Ibáñez, P. Geiregat, G. Nedelcu, A. Perea, E. Rodríguez-Cañecillas, R. Cordoba, M. V. Kovalenko, Z. Hens, *Chem. Mater.* **2020**, *32*, 5410; b) Q. A. Akkerman, G. Rainò, M. V. Kovalenko, L. Manna, *Nat. Mater.* **2018**, *17*, 394.

[5] a) J. Ding, S. Du, Z. Zuo, Y. Zhao, H. Cui, X. Zhan, *J. Phys. Chem. C* **2017**, *121*, 4917; b) B. Li, Y. Zhang, L. Zhang, L. Yin, L. Yin, *J. Power Sources* **2017**, *360*, 11.

[6] a) J. Pan, Y. Shang, J. Yin, M. De Bastiani, W. Peng, I. Dursun, L. Sinatra, A. M. El-Zohry, M. N. Hedhili, A.-H. Emwas, O. F. Mohammed, Z. Ning, O. M. Bakr, *J. Am. Chem. Soc.* **2018**, *140*, 562; b) J. Pan, L. N. Quan, Y. Zhao, W. Peng, B. Murali, S. P. Sarmah, M. Yuan, L. Sinatra, N. M. Alyami, J. Liu, E. Yassitepe, Z. Yang, O. Voznyy, R. Comin, M. N. Hedhili, O. F. Mohammed, Z. H. Lu, D. H. Kim, E. H. Sargent, O. M. Bakr, *Adv. Mater.* **2016**, *28*, 8718.

[7] L. M. Wheeler, E. M. Sanehira, A. R. Marshall, P. Schulz, M. Suri, N. C. Anderson, J. A. Christians, D. Nordlund, D. Sokaras, T. Kroll, S. P. Harvey, J. J. Berry, L. Y. Lin, J. M. Luther, *J. Am. Chem. Soc.* **2018**, *140*, 10504.

[8] Y.-H. Kim, G.-H. Lee, Y.-T. Kim, C. Wolf, H. J. Yun, W. Kwon, C. G. Park, T.-W. Lee, *Nano Energy* **2017**, *37*, 51.

[9] J. Park, H. M. Jang, S. Kim, S. H. Jo, T.-W. Lee, *Trends Chem.* **2020**, *2*, 785.

[10] a) J. Kim, Y. Lee, J. Lee, J. Kim, Y. Lee, B. Kim, J. Lee, B. Kim, *ACS Energy Lett.* **2021**, *6*, 2395; b) E. T. Vickers, T. A. Graham, A. H. Chowdhury, B. Bahrami, B. W. Dreskin, S. Lindley, S. Bonabi Naghadeh, Q. Qiao, J. Z. Zhang, *ACS Energy Lett.* **2018**, *3*, 2931.

[11] a) S. Lee, C. H. Jang, T. L. Nguyen, S. H. Kim, K. M. Lee, K. Chang, S. S. Choi, S. K. Kwak, H. Y. Woo, M. H. Song, *Adv. Mater.* **2019**, *31*, 1900067; b) E. D. Jung, A. K. Harit, D. H. Kim, C. H. Jang, J. H. Park, S. Cho, M. H. Song, H. Y. Woo, *Adv. Mater.* **2020**, *32*, 2002333; c) C. H. Jang, A. K. Harit, S. Lee, S. H. Kim, J.-E. Jeong, J. H. Park, E. D. Jung, J. M. Ha, S. K. Kwak, H. Y. Woo, M. H. Song, *ACS Nano* **2020**, *14*, 13246.

[12] a) D. Sarkar, A. Stelmakh, A. Karmakar, M. Aebli, F. Krieg, A. Bhattacharya, S. Pawsey, M. V. Kovalenko, V. K. Michaelis, *ACS Nano* **2024**, *18*, 21894; b) Y. Shynkarenko, M. I. Bodnarchuk, C. Bernasconi, Y. Berezovska, V. Verteletskyi, S. T. Ochsenbein, M. V. Kovalenko, *ACS Energy Lett.* **2019**, *4*, 2703; c) J.-H. Park, A. Lee, J. C. Yu, Y. S. Nam, Y. Choi, J. Park, M. H. Song, *ACS Appl. Mater. Interfaces* **2019**, *11*, 8428; d) M. Imran, P. Ijaz, L. Goldoni, D. Maggioni, U. Petralanda, M. Prato, G. Almeida, I. Infante, L. Manna, *J. Phys. Chem. Lett.* **2020**, *11*, 2079.

[13] a) Y. Zhang, H. Shaikh, A. J. Sneyd, J. Tian, J. Xiao, A. Blackburn, A. Rao, R. H. Friend, I. Manners, *J. Am. Chem. Soc.* **2021**, *143*, 7032; b) C. Cueto, M. Hu, T. P. Russell, T. Emrick, *J. Am. Chem. Soc.* **2024**, *146*, 8189.

[14] a) H.-F. Chen, C.-T. Liao, T.-C. Chen, H.-C. Su, K.-T. Wong, T.-F. Guo, *J. Mater. Chem.* **2011**, *21*, 4175; b) A. G. N. de Souza, Y. B. da Silva, R. R. Rodrigues, A. S. Menandro, L. O. Péres, *Macromol. Res.* **2024**, *32*, 757.

[15] B. R. Bennett, J. Chang, A. J. Bard, *Electrochim. Acta* **2016**, *219*, 1.

[16] a) M. Zhang, Q. Chen, R. Xue, Y. Zhan, C. Wang, J. Lai, J. Yang, H. Lin, J. Yao, Y. Li, L. Chen, Y. Li, *Nat. Commun.* **2019**, *10*, 4593; b) J. Miao, Z. Hu, M. Liu, M. Umair Ali, O. Goto, W. Lu, T. Yang, Y. Liang, H. Meng, *Org. Electron.* **2018**, *52*, 200; c) A. Lee, J. Kim, D. Lee, M. H. Song, *ACS Appl. Electron. Mater.* **2023**, *5*, 5325.

[17] J. Zhu, Y. Zhu, J. Huang, Y. Gong, J. Shen, C. Liu, *J. Mater. Chem. C* **2019**, *7*, 7201.

[18] S. Liu, W. Akram, F. Ye, J. Jin, F. Niu, S. Ahmed, Z. Ouyang, S.-C. Dong, G. Li, *ChemOpen* **2024**, *13*, 202400118.

[19] a) K. D. Wegner, P. T. Lanh, T. Jennings, E. Oh, V. Jain, S. M. Fairclough, J. M. Smith, E. Giovanelli, N. Lequeux, T. Pons, N. Hildebrandt, *ACS Appl. Mater. Interfaces* **2013**, *5*, 2881; b) Z. Liang, M. Kang, G. F. Payne, X. Wang, R. Sun, *ACS Appl. Mater. Interfaces* **2016**, *8*, 17478.

[20] a) A. Daineka, S. Seyidov, O. Selig, M. P. Hautzinger, A. Loiudice, M. Burian, F. Palazon, M. V. Kovalenko, M. I. Bodnarchuk, M. Petrović, V. W. Bergmann, S. A. L. Weber, A. Sepe, *Nat. Commun.* **2022**, *13*, 831; b) B. Yin, J. Cavin, D. Wang, D. Khan, M. Shen, C. Laing, R. Mishra, S. M. Sadeghi, *Chem. Mater.* **2020**, *32*, 8877; c) T. Galle, A. Katre, S. de Koster, J. C. van der Bok, F. Krieg, M. A. Loi, A. J. Houtepen, *ACS Appl. Energy Mater.* **2022**, *5*, 5415.

[21] C. Fang, I. Muhammad, P. Lea, M. Salerno, M. Prato, *Mater. Res. Bull.* **2020**, *137*, 111107.

[22] Y. Liu, Q. Xie, Y. Ying, Z. Gao, X. Shao, W. Xia, M. Zhou, W. Pei, X. Tang, Y. Tu, *Chem. Eng. J.* **2024**, *498*, 155515.

[23] P. Li, Y. Zhang, C. Liang, G. Xing, X. Liu, F. Li, X. Hu, G. Shao, Y. Song, *Adv. Mater.* **2018**, *30*, 1805323.

[24] S. Govinda, B. P. Kore, M. Bokdam, P. Mahale, A. Kumar, S. Pal, B. Bhattacharyya, J. Lahnsteiner, G. Kresse, C. Franchini, A. Pandey, D. D. Sarma, *J. Phys. Chem. Lett.* **2017**, *8*, 4113.